JM PAPERS

CrossMark

The *Pr*-dependence of the critical roughness height in two-dimensional turbulent Rayleigh–Bénard convection

Jian-Lin Yang[1], Yi-Zhao Zhang[1], Tian-cheng Jin[1], Yu-Hong Dong[1], Bo-Fu Wang[1] and Quan Zhou[1],†

[1]Shanghai Key Laboratory of Mechanics in Energy Engineering, Shanghai Institute of Applied Mathematics and Mechanics, School of Mechanics and Engineering Science, Shanghai University, Shanghai, 200072, PR China

We carry out direct numerical simulations of turbulent Rayleigh–Bénard convection in a square box with rough conducting plates over the Rayleigh number range $10^7 \leqslant Ra \leqslant 10^9$ and the Prandtl number range $0.01 \leqslant Pr \leqslant 100$. In Zhang *et al.* (*J. Fluid Mech.*, vol. 836, 2018, R2), it was reported that while the measured Nusselt number *Nu* is enhanced at large roughness height h, the global heat transport is reduced at small h. The division between the two regimes yields a critical roughness height h_c, and we now focus on the effects of the Prandtl number (Pr) on h_c. Based on the variations of h_c, we identify three regimes for $h_c(Pr)$. For low Pr, thermal boundary layers become thinner with increasing Pr. This makes the boundary layers easier to be disrupted by rough elements, leading to the decrease of h_c with increasing Pr. For moderate Pr, the corner-flow rolls become much more pronounced and suppress the global heat transport via the competition between the corner-flow rolls and the large-scale circulation (LSC). As a consequence, h_c increases with increasing Pr due to the intensification of the corner–LSC competition. For high Pr, the convective flow transitions to the plume-controlled regime. As the rough elements trigger much stronger and more frequent plume emissions, h_c again decreases with increasing Pr.

Key words: Bénard convection, turbulent convection

1. Introduction

As a typical fluid flow phenomenon, turbulent thermal convection that is driven by the temperature gradient occurs ubiquitously in nature. For example, it plays a crucial role in the atmospheric and oceanic circulations, the Earth's mantle movement, the formation

† Email address for correspondence: qzhou@shu.edu.cn

of the geomagnetic field, as well as numerous industrial applications. A paradigmatic model to study this kind of flow is turbulent Rayleigh–Bénard (RB) convection (Ahlers, Grossmann & Lohse 2009; Lohse & Xia 2010; Chillà & Schumacher 2012; Sun & Zhou 2014), i.e. the motion of a fluid layer sandwiched between two horizontal conducting plates heated from below and cooled from above. From a fundamental point of view, a key issue for turbulent RB convection is to reveal the relationship between the global heat-transfer efficiency, which is expressed in terms of the Nusselt number

$$Nu = \frac{Q}{\chi \Delta / H}, \tag{1.1}$$

and the control parameters of the system, called the Rayleigh number Ra and the Prandtl number Pr, namely

$$Ra = \frac{\alpha g \Delta H^3}{\nu \kappa} \quad \text{and} \quad Pr = \frac{\nu}{\kappa}, \tag{1.2a,b}$$

where Q is the transported heat flux across the fluid layer of height H for an applied temperature difference Δ, g is the gravitational acceleration, χ, α, ν and κ are the thermal conductivity, thermal expansion coefficient, kinematic viscosity and thermal diffusivity of the working fluid, respectively. Some of the earliest systematic studies and important theories (Malkus 1954; Priestly 1954; Kraichnan 1962; Howard 1963; Spiegel 1971) focused on this issue, and have stimulated many experimental (Xia, Xin & Tong 1995; Xin, Xia & Tong 1996; Xia, Lam & Zhou 2002; du Puits, Resagk & Thess 2010; Roche *et al.* 2010; He *et al.* 2012; Bao *et al.* 2015; Lepot, Aumaître & Gallet 2018; Wang, Mathai & Sun 2019; Zhu *et al.* 2019a), numerical (Verzicco & Camussi 1999; Silano, Sreenivasan & Verzicco 2010; Stevens, Lohse & Verzicco 2011; Huang & Zhou 2013; Kaczorowski & Xia 2013; van der Poel, Stevens & Lohse 2013; Pandey & Verma 2016; Zwirner & Shishkina 2018; Wang, Zhou & Sun 2020) and theoretical (Dubrulle 2002; Grossmann & Lohse 2004, 2011; Whitehead & Doering 2011; Shishkina *et al.* 2015) investigations in the past several decades. Among these studies, the scaling relation has been widely used to describe the dependence $Nu(Ra, Pr)$ (see, Ahlers *et al.* (2009); Chillà & Schumacher (2012), for recent reviews).

Although thermal convection is believed to be an effective means to transport heat via a moving fluid – it carries upwards a heat flux which is normally many times larger than that by thermal diffusion – the turbulent heat-exchange efficiency is vastly limited by thermal diffusion in the boundary layers (BLs). As the enhancement of heat transfer is of fundamental interest and especially useful in many thermal engineering processes, some strategies have been put forward to overcome the BL limitation and to achieve high heat flux. Among these methods, the introduction of wall roughness is the most widely used one (Roche *et al.* 2001; Qiu, Xia & Tong 2005; Tisserand *et al.* 2011; Wei *et al.* 2014; Liot *et al.* 2017; Xie & Xia 2017; Jiang *et al.* 2018; Rusaouen *et al.* 2018; Foroozani *et al.* 2019; Zhu *et al.* 2019b). For instance, Du & Tong (1998, 2000) experimentally observed that rough surfaces could enhance the detachment of the thermal BL from the tips of rough elements, and hence the heat transport across the cell with rough upper and lower surfaces is increased by more than 76 %. Numerical results of Stringano, Pascazio & Verzicco (2006) and Salort *et al.* (2014) also reported an increase of heat transfer when the mean thermal BL thickness becomes smaller than the roughness height. In a cylindrical cell with a set of isothermal obstacles attached to the plates, Emran & Shishkina (2020) recently showed that the global heat flux can be several times that in the traditional smooth cell when the obstacle rings are very tall and the gaps between them are sufficiently wide. On the other aspect, Ciliberto & Laroche (1999) experimentally found that the scaling

exponent of heat transport between Nu and Ra increases if the roughness has power-law distributed heights and the thermal BL thickness is smaller than the maximum roughness size. With sinusoidally rough upper and lower surfaces in two dimensions, Toppaladoddi, Succi & Wettlaufer (2015, 2017) numerically showed that the $Nu(Ra)$ scaling exponent reaches the value of 0.5 for a certain roughness wavelength. Recent studies (Zhu *et al.* 2017; MacDonald *et al.* 2019; Emran & Shishkina 2020) further revealed that at height Ra the $Nu(Ra)$ exponent decreases back to the exponent in the smooth cell, due to the competition between the turbulent bulk and BL flow.

Nevertheless, when looking closely into the results in the literature, some data (Stringano *et al.* 2006; Zhu *et al.* 2017) seem to suggest that surface roughness would also reduce the global heat transport through the convection system. Indeed, Shishkina & Wagner (2011) argued that when the distances between rough elements are very small, a reduction of the resulting Nu is possible due to the decrease of the effective Ra. In a previous work, we systematically investigated $Nu(h)$ in both two-dimensional (2-D) and three-dimensional (3-D) cells with rough elements of height h (Zhang *et al.* 2018). Our results revealed that when h is small or Ra is low, the global heat transport may be suppressed as the hot/cold fluid is trapped and accumulates inside the cavity regions between the adjacent rough elements, leading to much thicker thermal BLs in these regions. On the other hand, when h is large or Ra is high enough, the large-scale circulation (LSC) in the bulk can penetrate into the cavities, vigorously mixing the trapped hot/cold fluid, and thus significantly improving the heat-exchange efficiency of the system. The division between these two regimes (i.e. the Nu-reduction and Nu-enhancement regimes) then gives a critical roughness height h_c, at which $Nu(h)$ crosses the value of $Nu(h = 0)$ of the smooth cell.

As a typical length scale for the convective heat transfer, h_c denotes the onset of the Nu-enhancement induced by rough surfaces. Therefore, it is of great interest and fundamental importance to reveal its dependence on the control parameters of the system, such as $h_c(Ra, Pr)$. Our previous results have shown that h_c decreases with growing Ra as $h_c \sim Ra^{-0.6}$. The objective of the present paper is to reveal the Pr effects on h_c with the help of direct numerical simulations of turbulent thermal convection in a 2-D square box. Note that the Pr-dependence in three dimensions may be different from that in two dimensions, as the observed phenomenon at low to intermediate Pr could be different in three dimensions (van der Poel *et al.* 2013). The paper is organized as follows. Section 2 gives a brief description of the governing equations and numerical methods adopted. The Pr-dependence of h_c is discussed and analysed in § 3, where we try to understand the mechanism that dominates the observed $h_c(Pr)$ relation in three different Pr regimes. Finally, we summarize our results in § 4.

2. Numerical methods

The coupled equations of motion for the velocity field $\boldsymbol{u}$ ($= u\boldsymbol{x} + w\boldsymbol{z}$) and the temperature field θ in the Oberbeck–Boussinesq approximation of turbulent thermal convection are numerically solved,

$$\nabla \cdot \boldsymbol{u} = 0, \tag{2.1}$$

$$\partial_t \boldsymbol{u} + (\boldsymbol{u} \cdot \nabla)\boldsymbol{u} = -\nabla p + \sqrt{\frac{Pr}{Ra}}\nabla^2 \boldsymbol{u} + \theta \boldsymbol{z}, \tag{2.2}$$
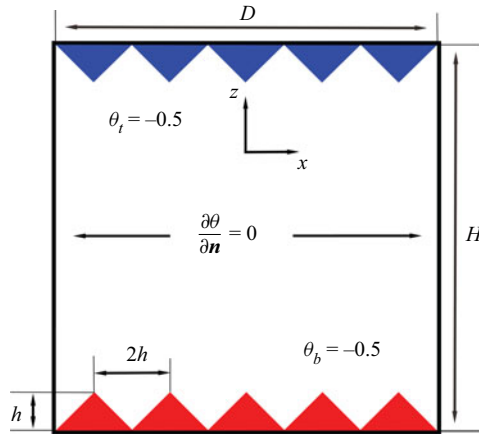
Figure 1. A sketch of the 2-D convection cell with the coordinate system. Right-triangular rough elements with a vertex angle of $90°$, height h and base width $2h$ are located on either of the conducting plates.

$$\partial_t \theta + (\boldsymbol{u} \cdot \boldsymbol{\nabla})\theta = \sqrt{\frac{1}{RaPr}} \nabla^2 \theta, \qquad (2.3)$$

where p is the kinematic pressure field and $\boldsymbol{x}$ and $\boldsymbol{z}$ are, respectively, the unit vectors in the horizontal and vertical directions. The equations have been non-dimensionalized with respect to the cell height H, the imposed temperature difference across the cell Δ and the free-fall velocity $\sqrt{\alpha g \Delta H}$.

The convection cell adopted is a 2-D square box of height $H = 1$, width $D = 1$ and aspect ratio $\Gamma = D/H = 1$. As shown in figure 1, the triangular rough elements with a vertex angle of $90°$, height h and base width $2h$ are located on both of the upper and lower conducting plates. To study the effects of surface roughness on the global heat transport, we systematically vary the roughness height h. For such roughness geometry, the contact area of the rough surface is 41 % larger than the smooth surface and does not change with the roughness height h. Hence, the contact area does not contribute to the variations in the measured Nu when changing h. In the present study, we simulate over the parameter ranges $10^7 \leqslant Ra \leqslant 10^9$ and $0.01 \leqslant Pr \leqslant 100$, mainly focusing on the effects of the Prandtl number Pr on the global heat transport through the RB system with rough surfaces. At least 10 individual simulations with different h_c were carried out for each set of (Ra, Pr), and a total of more than 400 independent realizations of 2-D turbulent RB convection with rough surfaces have been performed in the present study.

During the simulations, the temperatures of the upper and lower conducting plates are fixed at $\theta_t = -0.5$ and $\theta_b = 0.5$, respectively, while the vertical sidewalls are thermally insulated (i.e. $\partial \theta / \partial \boldsymbol{n} = 0$). No-slip boundary conditions are applied at all solid surfaces for the velocity field. In our numerical code, a fourth-order finite-difference scheme with staggered grids is adopted to solve the governing equations and an immersed boundary method is applied to deal with the boundaries of rough elements. Non-equidistant meshes are implemented and the computational meshes are refined close to all solid walls so that the thermal and viscous BLs near the rough surfaces are, respectively, resolved with at least 16 and 15 grid points for all runs.

Our numerical code has been extensively used in previous studies (Bao *et al.* 2015; Zhang *et al.* 2018, 2019). Here, to further validate the code, we compare in figure 2(*a*) the measured Nusselt number Nu as a function of the Prandtl number Pr obtained at $Ra = 10^8$
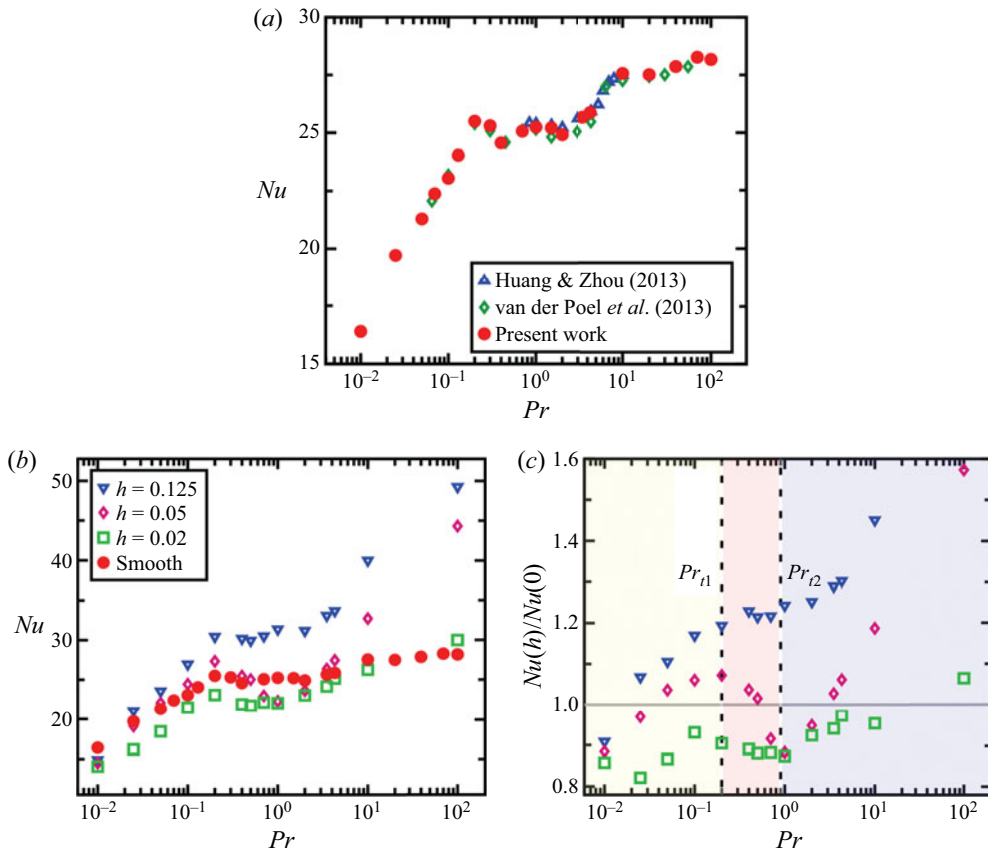
911 A52-4

Figure 2. (*a*) The Nusselt number *Nu* as a function of *Pr* obtained in the smooth cell at $Ra = 10^8$. For comparison, we also plot the data from Huang & Zhou (2013) (triangles) and van der Poel *et al.* (2013) (diamonds). (*b*) The Nusselt number *Nu* as a function of *Pr* at $Ra = 10^8$ obtained in the smooth cell and rough cells of three typical roughness heights $h = 0.02$, 0.05 and 0.125. (*c*) The corresponding ratio $Nu(h)/Nu(0)$ as a function of *Pr*. The data are the same as those in panel (*b*). Different colours mark the three regimes and the two dashed lines indicate the two transitional Prandtl numbers, Pr_{t1} and Pr_{t2}, obtained at $Ra = 10^8$.

in the smooth cell with those of Huang & Zhou (2013) and van der Poel *et al.* (2013). Although the dependence between *Nu* and *Pr* seems to be a bit complicated, excellent agreement among the three data sets can be clearly observed, illustrating the good quality of the present simulations. We further note that the Nusselt number of the smooth cell we measure ($Nu = 50.85$ at $Ra = 10^9$ and $Pr = 1$) is in agreement with the one computed using the open-source code Nek5000 by Xu *et al.* (2018) ($Nu = 50.833$) to a precision of less than 1 %.

3. Results and discussion

We first examine the Nusselt number *Nu*, which is calculated as

$$Nu = \sqrt{PrRa}\langle w\theta \rangle - \langle \partial_z \theta \rangle, \tag{3.1}$$

where *w* is the vertical velocity, ∂_z is the vertical derivative and $\langle \cdot \rangle$ indicates the average over time and over the midheight horizontal plane. The temporal average is performed over a duration of more than 500 dimensionless time units after the convective flow in the

system has been fully developed. The time convergence of Nu is checked by comparing the time-averages over the first and the last halves of the simulation, and the resulting error is smaller than 2 % for all runs.

In figure 2(*b*) we show a semilog plot of the numerically measured Nu versus the Prandtl number Pr obtained in rough cells of three typical heights $h = 0.02$, 0.05 and 0.125. For comparison, the global convective heat flux through a smooth cell, $Nu(h = 0)$, is also plotted. In general, the heat-transfer efficiency is enhanced with increasing Pr. For most values of Pr studied, $Nu(h)$ is higher than that of the smooth cell for large roughness height (e.g. $h = 0.125$, blue down-triangles), and is lower than the corresponding $Nu(0)$ for small h (e.g. $h = 0.02$, green squares). The situation for medium roughness height (e.g. $h = 0.05$, pink diamonds) seems to be more complicated. To better compare the data, we adopt $Nu(0)$ of the smooth cell to normalize $Nu(h)$ of the rough cells, and the corresponding results are displayed in figure 2(*c*). Clearly, the data of $h = 0.05$ exhibit a zigzag dependence on Pr, i.e. $Nu(h)/Nu(0)$ is an increasing function for small or large Pr and is a decreasing function for intermediate Pr. As discovered by Zhang *et al.* (2018), there is a critical roughness height h_c: $Nu(h)/Nu(0) > 1$ for $h > h_c$, while $Nu(h)/Nu(0) < 1$ for $h < h_c$. The zigzag behaviours of $Nu(h)/Nu(0)$ on Pr thus imply a complicated Pr-dependence of h_c. Indeed, as we shall see below, the zigzag behaviour of the $h = 0.05$ data exactly coincides with the three regimes of $h_c(Pr)$.

The normalized Nusselt number, $Nu(h)/Nu(0)$, is plotted in figure 3(*a,c,e*) as a function of the roughness height h for several values of Pr varying from 0.01 to 100. Similar to our previous results at fixed $Pr = 0.7$ (Zhang *et al.* 2018), the data sets of all Pr studied can be divided into two regimes: the Nu-reduction regime at small h and the Nu-enhancement regime at large h. The crossover between these two regimes thus yields a critical roughness height h_c, at which $Nu(h_c) = Nu(h = 0)$, denoting the onset of Nu-enhancement induced by rough surfaces. The dashed lines in figure 3(*e*) illustrate how h_c is obtained in our simulations. Specifically, a linear function is used to fit the data of $Nu(h)$ around $Nu(h)/Nu(0) = 1$, and then the critical roughness height h_c is determined by the crossing between the fitting and the value of unity. It is clearly seen that h_c varies with Pr, i.e. h_c is in general large for low Pr, but small for high Pr. Furthermore, the overall magnitudes of Nu for high Pr are in general larger than those for low Pr, i.e. the Nu-reduction is more pronounced and the Nu-enhancement is much weaker for low Pr. Therefore, the Nu-reduction problem induced by surface roughness becomes more relevant for low Pr. For moderate Pr, on the other hand, the dependence of h_c on Pr seems to be a bit complicated. Note that $Nu(h)/Nu(0)$ varies non-monotonically with h for $h > h_c$. As argued by Zhu *et al.* (2017) and Zhang *et al.* (2018), this may be caused by the transition from the bulk-controlled regime to the BL-dominated regime with the increasing roughness size.

To compare $Nu(h)$ obtained at different Pr, we use h_c to normalize the data, and the corresponding results are plotted in figure 3(*b,d,f*). Unlike our previous results which show a nearly universal profile between $Nu(h)/Nu(0)$ and h/h_c for different Ra (Zhang *et al.* 2018), the symbols for different Pr cannot collapse well on top of each other. This discrepancy is a result of the different regimes, i.e. the convective flow in different Pr-regimes is governed by different dynamics.

In order to reveal the detailed relation between h_c and Pr, we plot in figure 4 the measured h_c as a function of Pr for three Ra. The value of h_c decreases with increasing Pr for too small and too large Pr, but increases with ascending Pr for medium Pr. Based on the observed $h_c(Pr)$ relation, one can identify three flow regimes, which are marked by different colours as shown in figure 4. As we shall see below, the three regimes are
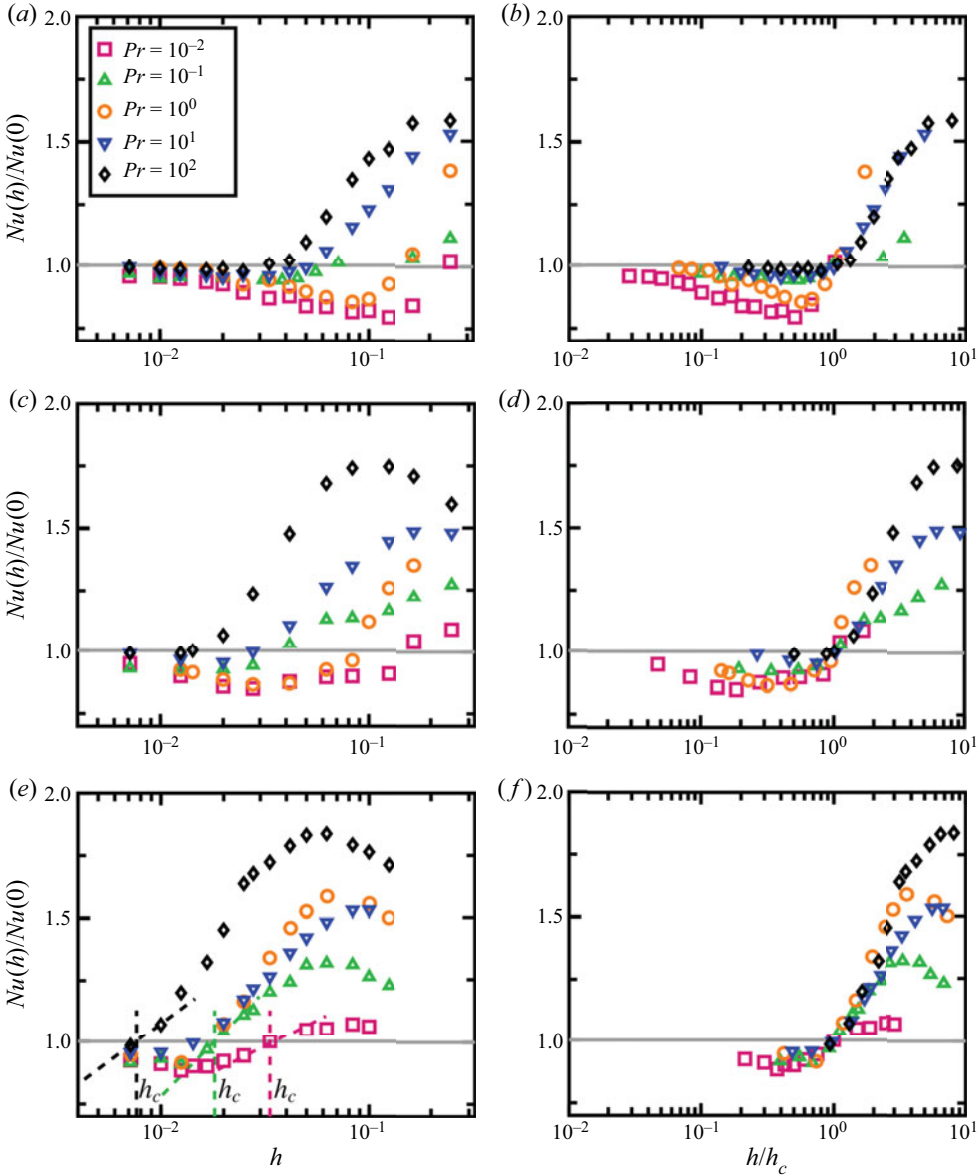
Figure 3. The ratio $Nu(h)/Nu(0)$ as a function of (a,c,e) h and (b,d,f) h/h_c obtained at (a,b) $Ra = 10^7$, (c,d) $Ra = 10^8$ and (e,f) $Ra = 10^9$ for Pr varying from 0.01 to 100. The dashed lines in panel (e) show the determination of the critical roughness height h_c at which $Nu(h)/Nu(0) = 1$.

governed by different flow dynamics, and can be referred to the LSC-controlled regime, the corner–LSC-competition regime and the plume-controlled regime, respectively.

It should be noted that based on dimensional analysis, our previous work (Zhang *et al.* 2018) yielded a scaling relation between h_c and the Reynolds number Re, i.e. $h_c \sim Re^{-1}$, by assuming a balance between the inertial and viscous forces. This, taken together with the results of $Re \sim Pr^{-0.88 \pm 0.04}$ in § 3.4, one obtains $h_c \sim Pr^{0.88}$. In figure 4, we plot this scaling as the solid line for reference. It is clearly seen that the scaling is a good
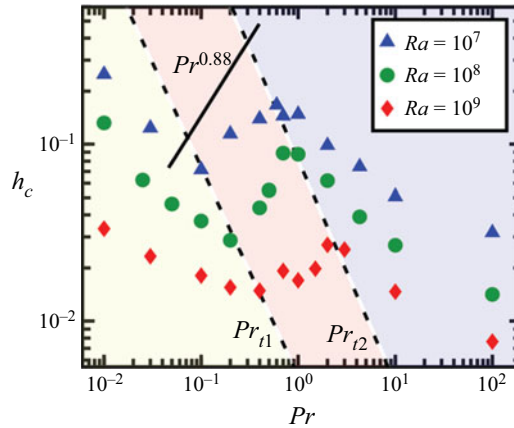
Figure 4. Log–log plot of the critical roughness height h_c as a function of Pr obtained at $Ra = 10^7$ (triangles), $Ra = 10^8$ (circles) and $Ra = 10^9$ (diamonds). Three flow regimes can be separated by two transitional Prandtl numbers, Pr_{t1} and Pr_{t2}, and indicated by different colours: the LSC-controlled regime (yellow), the corner–LSC-competition regime (pink) and the plume-controlled regime (cyan). The solid line indicates the scaling $h_c \sim Re^{-1} \sim Pr^{0.88}$ (Zhang *et al.* 2018) for reference.

description for the data at $Ra = 10^8$, but the data at $Ra = 10^7$ and 10^9 are less well described by this trend, which indicates that the dynamics are not as simple as suggested by the previous dimensional analysis. Indeed, a much more complicated zigzag dependence of $h_c(Pr)$ is obtained in the present study. The reason for this discrepancy may be due to the fact that thermal effects (or the plume dynamics) are not considered in the previous dimensional analysis. As we shall see below, the plume dynamics plays a central role in the transitions among the three regimes. In the remainder of this paper, we will focus on the flow dynamics in each regime.

3.1. *The LSC-controlled regime*

We next focus on the low-Pr regime. Figure 5(*a,b*) shows the time-averaged temperature and velocity fields obtained at $Ra = 10^8$ and $Pr = 0.01$ in the smooth cell and in the rough cell with $h = 0.05$, respectively. The mean dominant flow pattern is a square-like anticlockwise rotatory motion. From the corresponding movie, one can also see some smaller secondary rolls at the corners of the cell. In this low-Pr regime, however, these corner-flow rolls are not stable and could detach from the corners and hence are not pronounced in the mean flow field, as shown in figure 5(*a*). This is because the corner-flow rolls are energetically fed by thermal plumes that are emitted from thermal BLs (Sugiyama *et al.* 2010). But at low Pr (i.e. for large thermal diffusivity), thermal plumes are hardly being generated (Verzicco & Camussi 1999), since they can much more easily lose their thermal energy through thermal diffusion. Therefore, for low Pr, the flow is dominated by the single LSC, which we refer to as the LSC-controlled regime.

To understand the behaviour of $h_c(Pr)$ in the LSC-controlled regime, we note that the global heat flux through the RB system is depressed for too small Pr. Indeed, as revealed by figure 2(*a*), Nu decreases from 25.5 at $Pr = 0.2$ to 16.4 at $Pr = 0.01$. The decrease in heat transport for a given Ra as Pr drops has already been observed in previous numerical (Verzicco & Camussi 1999; Scheel & Schumacher 2016; Zwirner & Shishkina 2018; Xu, Shi & Xi 2019) and experimental (Horanyi, Krebs & Müller 1999; Xia *et al.* 2002; Frick *et al.* 2015) studies. The reason for such a decrease in $Nu(Pr)$, as argued by Grossmann
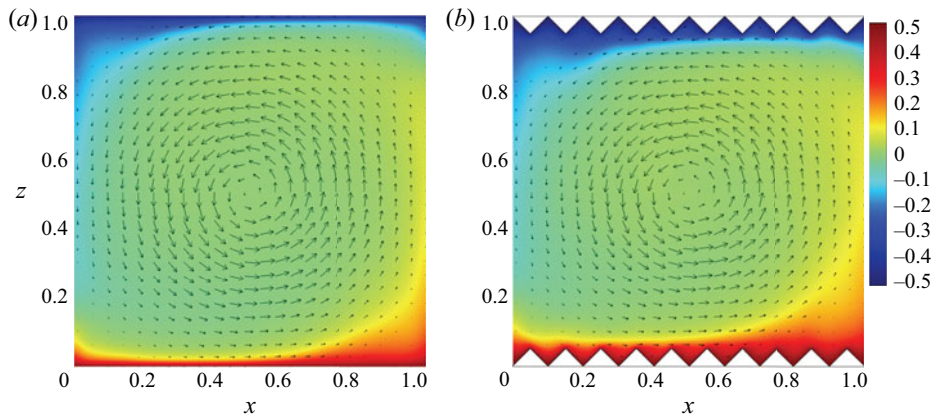
Figure 5. Snapshots of the time-averaged temperature (colour) and velocity (arrows) fields at $Ra = 10^8$ and $Pr = 0.01$ in the LSC-controlled regime obtained (*a*) in the smooth cell and (*b*) in the rough cell with $h = 0.05$ (the *Nu*-reduction regime). The corresponding movie is provided in the supplementary material available at https://doi.org/10.1017/jfm.2020.1091.

& Lohse (2004, 2008), is that the convective flow at low Prandtl numbers is dominated by molecular transport, and correspondingly does not significantly contribute to the global heat transport.

As the convective heat transport is mainly determined by the conductive thermal BLs in the classical regime of turbulent thermal convection, the decrease in $Nu(Pr)$ with descending Pr means the thickening of thermal BLs. Figure 6(*a*) shows the mean thermal BL thickness δ_{th}^0, estimated using $\delta_{th}^0 = 1/[2Nu(0)]$, as a function of Pr obtained in the smooth cell at $Ra = 10^8$. Here, only part of the data is shown because we mainly focus on the flow dynamics in the low-Pr regime. It is illustrated that δ_{th}^0 is elevated with descending Pr in the LSC-controlled regime (i.e. the yellow-shaded area), as expected from the Nu data in figure 2(*a*). Figure 6(*b*) displays the local thermal BL thickness $\delta_{th}^0(x)$ along the lower plate obtained at three Pr in the smooth cell. Here, $\delta_{th}^0(x)$ is determined as the distance at which the tangent of the time-averaged temperature profile at the lower plate meets the bulk temperature (Zhou & Xia 2013). It is further illustrated that at low Prandtl numbers thermal BLs thicken with decreasing Pr. A thicker thermal BL would make the bulk flow harder to penetrate into the cavities between the rough elements and properly mix the trapped hot/cold fluid. Therefore, higher rough elements are needed to disrupt thermal BLs and enhance the global heat transport through the system, which leads to the increase of h_c with decreasing Pr in the LSC-controlled regime.

3.2. *The corner–LSC-competition regime*

With the increase in Pr (i.e. the decrease in thermal diffusivity), thermal plumes become more coherent and then detach from thermal BLs. Some of these plumes are trapped in the corner and provide energy to the corner flows. Correspondingly, some stable corner-flow rolls can be developed at medium Prandtl numbers. Figure 7(*a*) shows the time-averaged velocity and temperature fields at $Ra = 10^8$ and $Pr = 0.4$ in the smooth cell. As we can see, except for the dominant stadium-like LSC that is diagonally orientated in the cell, two smaller clockwise rolls are built up well at the two opposite corners. When the hot/cold fluids move upwards/downwards with the corner flows, they encounter and then compete with the LSC. Due to the relatively weak strength of the corner rolls, these hot/cold fluids
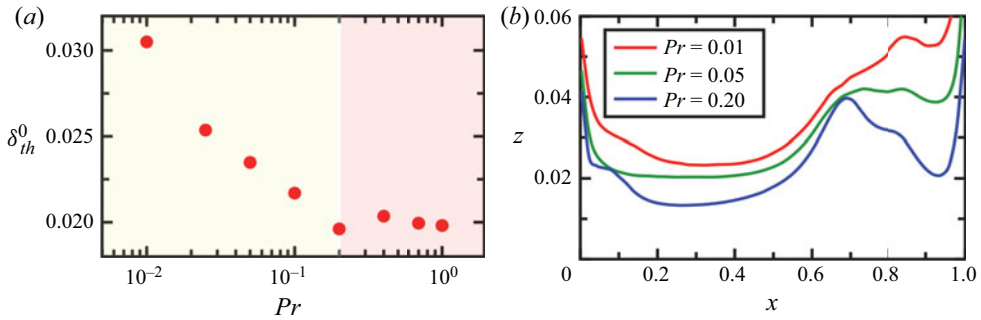
Figure 6. (a) The mean thermal BL thickness, δ_{th}^0, as a function of Pr obtained in the smooth cell at $Ra = 10^8$. Here, δ_{th}^0 is estimated using $\delta_{th}^0 = 1/[2Nu(0)]$. The yellow-shaded area corresponds to the LSC-controlled regime. (b) The local thermal BL thickness, $\delta_{th}^0(x)$, in the z-direction near the lower plate as a function of the horizontal position x obtained in the smooth cell at $Ra = 10^8$ and at three different Pr. Here, $\delta_{th}^0(x)$ is determined from the time-averaged temperature profiles using the 'slope' method (Zhou & Xia 2013).
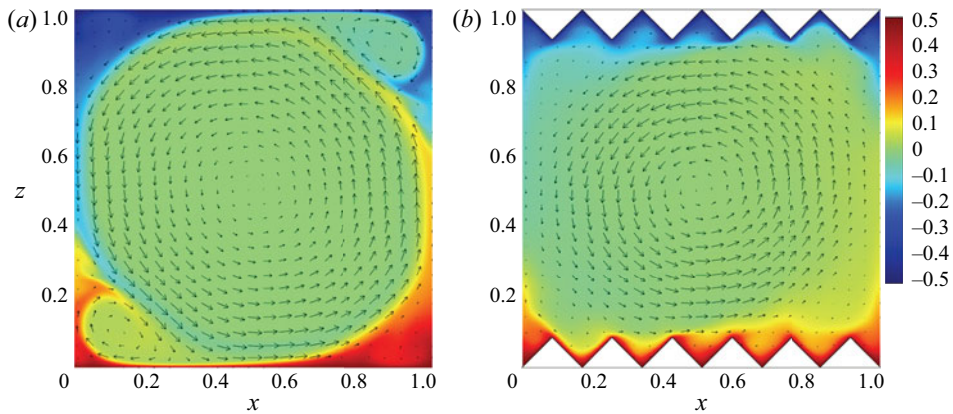

Figure 7. Snapshots of the time-averaged temperature (colour) and velocity (arrows) fields at $Ra = 10^8$ and $Pr = 0.4$ in the corner–LSC-competition regime obtained (a) in the smooth cell and (b) in the rough cell with $h = 0.0833$ (the Nu-enhancement regime). The corresponding movie is provided in the supplementary material.

are forced back to the hot/cold plates. This process gives rise to strong counter-gradient local heat flux that negatively contributes to the global heat transport (Huang & Zhou 2013). Such a competition also plays a crucial role in the flow dynamics of turbulent RB convection, such as the reversals of the LSC (Sugiyama *et al.* 2010; Chandra & Verma 2013). Therefore, for moderate Pr, there exists an intense competition between the corner-flow rolls and the LSC, which we refer to as the corner–LSC-competition regime.

When wall roughness is introduced into the system, more plumes are produced and erupted from the tips of rough elements (Du & Tong 1998, 2000), and then enter the convective bulk. A detailed observation of the supplementary movie corresponding to figure 7 reveals that these plumes interact with the large-scale flow structures in the bulk. When these plumes are strong enough (i.e. for rough elements high enough), they make the corner-flow rolls unstable. Figure 7(b) shows the time-averaged flow field obtained in a rough cell with $h = 0.0833$ in the Nu-enhancement regime. Unlike the smooth case (see figure 7a), the corner-flow rolls are dramatically suppressed in this rough case due to
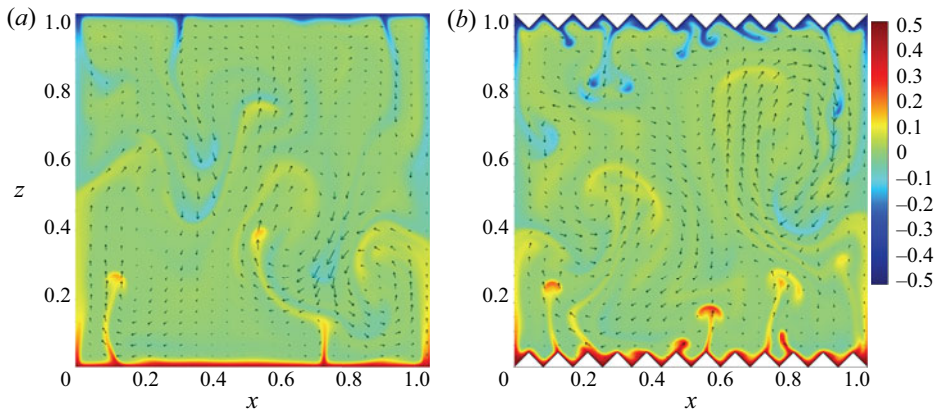
911 A52-10

Figure 8. Typical snapshots of the instantaneous temperature (colour) and velocity (arrows) fields at $Ra = 10^8$ and $Pr = 100$ in the plume-controlled regime obtained (*a*) in the smooth cell and (*b*) in the rough cell with $h = 0.0417$ (the *Nu*-enhancement regime). The corresponding movie is provided in the supplementary material.

the disturbance induced by the interaction of thermal plumes from the roughness tips. As stated above, the corner-flow rolls negatively contribute to the global heat transport via the corner–LSC competition, and thus the suppression of the corner flows would result in an enhancement of the heat-transfer efficiency of the system.

In the corner–LSC-competition regime, the increase of the critical roughness height h_c with Pr may be attributed to two effects. First, as Pr increases, the corner rolls grow in both kinetic energy and size and their strength becomes stronger (Sugiyama *et al.* 2010; Huang & Zhou 2013). Correspondingly, higher rough elements are needed to disrupt the stronger corner-flow rolls and suppress the counter-gradient heat transport induced by the corner–LSC competition. The second possible factor is that the flow inside the cavities between the rough elements becomes more viscous with the increase in Pr (i.e. the increase in kinematic viscosity). Accordingly, a larger roughness height is needed to vigorously mix the trapped hot/cold fluid within the cavity regions and achieve a heat-transport enhancement (Zhang *et al.* 2018).

3.3. *The plume-controlled regime*

As Pr continues to elevate, the Reynolds number decreases and the large-scale flows weaken due to the increase of fluid viscosity (Verzicco & Camussi 1999; Breuer *et al.* 2004). Then, thermal plumes become more dominant and are responsible for most of the heat transport (Shang, Tong & Xia 2008). Figure 8(*a,b*) shows typical snapshots of the instantaneous temperature and velocity fields at $Pr = 100$ in the smooth cell and in the rough cell with $h = 0.0417$, respectively. A corresponding video can be viewed as supplementary material. As we can see, thermal plumes are generated and erupted from thermal BLs at random positions (at random tips in rough cells). In the bulk region, they are fully developed with a well-defined spatial structure, and bring about a multicellular structure of the flow. Therefore, for high Pr, the flow is dominated by thermal plumes, which we refer to as the plume-controlled regime.

To physically understand why the critical roughness height h_c decreases with Pr in the plume-controlled regime, we look closely into the flow structures near the lower plate, as illustrated in figure 9. At medium Pr (figure 9*a*), the convective bulk is mainly controlled by large-scale flow structures, like the corner flows and the LSC, which sweep the upper
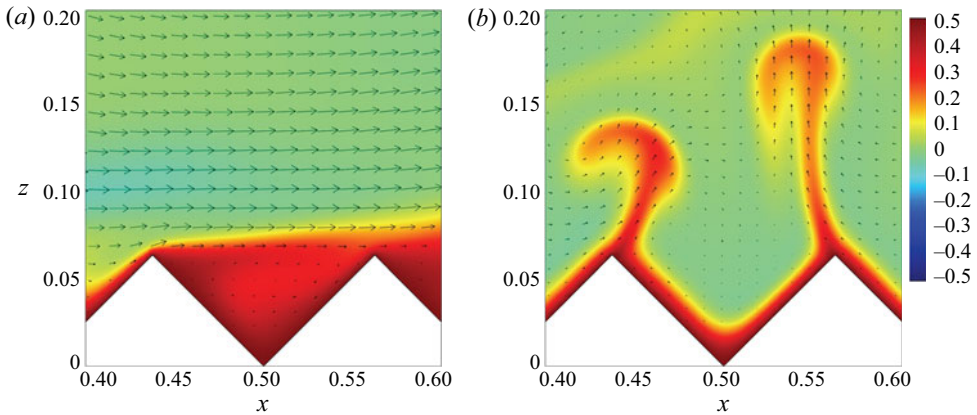
Figure 9. Typical snapshots of the instantaneous temperature (colour) and velocity (arrows) fields near the centre of the lower plate. The data are obtained in the rough cell with $h = 0.0625$ at $Ra = 10^8$ and at (a) $Pr = 1$ and (b) $Pr = 100$. The corresponding movie is provided in the supplementary material.

and lower horizontal plates. As the separation between the adjacent rough elements is not large enough, like the situation shown in figure 9(a), the large-scale flow cannot effectively penetrate into the cavity regions. This results in the accumulation of the hot/cold fluid in the cavities and correspondingly impedes the global heat flux, as revealed by Zhang *et al.* (2018). At high Pr (figure 9b), on the other hand, thermal dissipation is much slower than viscous dissipation. Thermal structures, like plumes, can thus sustain their thermal energy (i.e. keep their temperature higher/lower than the environment) for a long time. Under the effects of buoyant forces, these structures move upwards/downwards, carry and transfer most of the heat through the system. Since the rough elements can trigger the massive eruption of thermal plumes, they speed up this process. As shown in figure 9(b), the hot fluid moves upwards along the sides of rough elements and eventually forms thermal plumes and detaches from the rough tips, rather than being trapped inside the cavities. Therefore, at high Prandtl numbers, it is much easier for the roughness to produce thermal plumes and contribute to the Nu-enhancement, which leads to a small h_c for high Pr.

3.4. *Transitions among the three regimes*

According to the above discussions, thermal plumes play a crucial role in the transitions among the three h_c–Pr regimes. For too small Pr (i.e. the LSC-controlled regime), thermal plumes hardly appear due to large thermal diffusivity and the heat transport is mainly dominated by molecular transport (Grossmann & Lohse 2004, 2008). For medium Pr (i.e. the corner–LSC-competition regime), thermal plumes begin to be produced and detach from thermal BLs. After entering the bulk region, these plumes organize themselves into the large-scale flow structures (Xi, Lam & Xia 2004), like the corner-flow rolls and the LSC. For too large Pr (i.e. the plume-controlled regime), the large-scale flows weaken due to large fluid viscosity and most of the heat in the system is carried and transferred by thermal plumes. Taken together, there are two transitions among these three regimes; the first one corresponds to the emergence of thermal plumes, and the second one is due to the thermal plumes becoming dominant in the convective flow.

To confirm that the different regimes discussed above coincide with the transitions of $h_c(Pr)$ identified in figure 4, we note that there are stable corner-flow rolls for medium Pr (see figure 10b), while the corner rolls are less pronounced for too small (see figure 10a) or
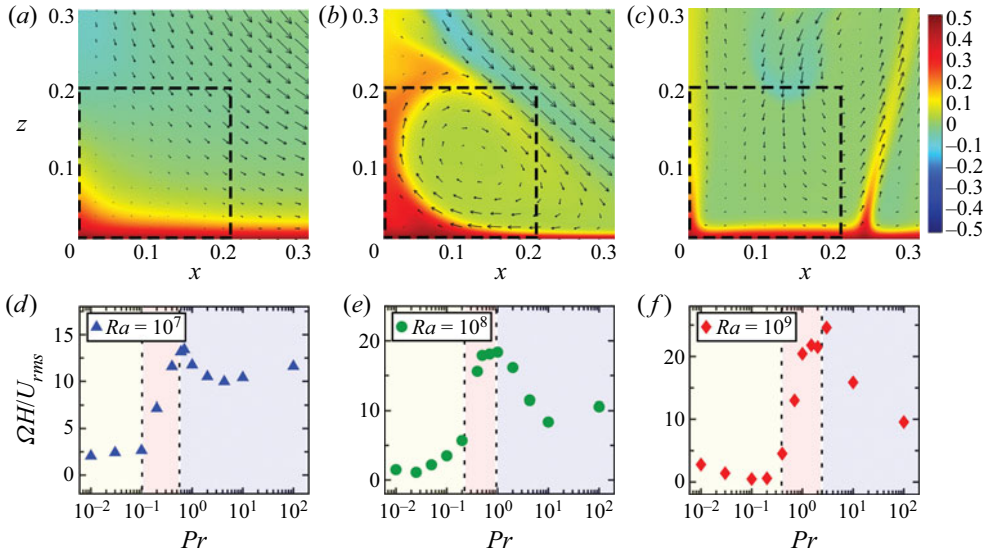
Figure 10. (*a–c*) Typical snapshots of the instantaneous temperature (colour) and velocity (arrows) fields in the lower-left corners of the smooth convection cell at $Ra = 10^8$ and at (*a*) $Pr = 0.01$ (the LSC-controlled regime), (*b*) $Pr = 0.4$ (the corner–LSC-competition regime) and (*c*) $Pr = 100$ (the plume-controlled regime). The dashed squares indicate the regimes where the angular velocity Ω of the lower-left corners is calculated. (*d–f*) The compensated angular velocity, $\Omega H/U_{rms}$, as a function of Pr obtained at (*d*) $Ra = 10^7$, (*e*) $Ra = 10^8$ and (*f*) $Ra = 10^9$. Different colours mark the three regimes identified from figure 4 and the dashed lines indicate the transitional Prandtl numbers at the corresponding Ra.

too large Pr (see figure 10*c*). To quantitatively characterize these flow states, we calculate the angular velocity in the lower-left corners as

$$\Omega = \left\langle \frac{u(x, z, t)}{z - 0.1H} - \frac{w(x, z, t)}{x - 0.1D} \right\rangle_{corner,t}, \tag{3.2}$$

where $\langle \cdots \rangle_{corner,t}$ denotes an average over time and over a spatial regime $0 < x < 0.2D$ and $0 < z < 0.2H$, as indicated by the dashed squares in figure 10(*a–c*). Based on this definition, a large magnitude of Ω corresponds to a stable corner-flow roll and thus signals the corner–LSC-competition regime, while the corner flow is weak and unstable when the magnitude of Ω is small. Figure 10(*d–f*) shows the measured Ω as a function of Pr, where Ω has been compensated by U_{rms}/H with $U_{rms} = \sqrt{\langle (u^2 + w^2) \rangle_{V,t}}$ being a typical root mean square (subscript rms) velocity of the system and $\langle \cdot \rangle_{V,t}$ being a space–time average. For comparison, different background colours of figure 10(*d–f*) mark the three regimes identified at the corresponding Ra in figure 4. For all three Ra studied, the magnitude of the compensated $\Omega H/U_{rms}$ is close to the value of zero in the LSC-controlled regime (the yellow-shaded area), as for small Pr the convective flow is dominated by a single large-scale wind and the corner-flow rolls are not stable and could detach from the corners. The magnitude of $\Omega H/U_{rms}$ raises rapidly in the corner–LSC-competition regime (the pink-shaded area), indicating that stable corner-flow rolls are well developed in this regime. In the plume-controlled regime (the cyan-shaded area), the value of $\Omega H/U_{rms}$ drops with increasing Pr, as both the LSC and the corner-flow rolls weaken for large Pr. Therefore, the flow analysis in figure 10(*d–f*) quantitatively verifies that the three regimes (i.e. the LSC-controlled, corner–LSC-competition and plume-controlled regimes) indeed correspond to the transitions of $h_c(Pr)$ identified in figure 4.
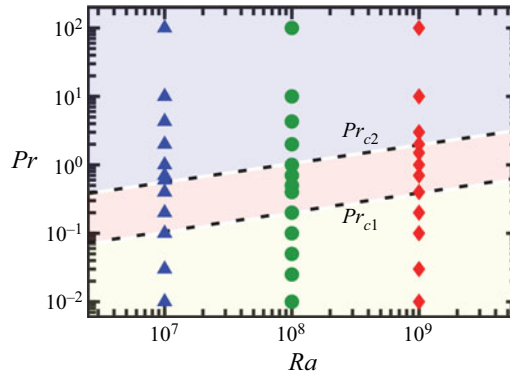
Figure 11. Explored phase diagram of different regimes in the Ra–Pr plane. The two dashed lines mark the transitional Prandtl numbers Pr_{t1} and Pr_{t2} that separate the three regimes. Here, Pr_{t1} and Pr_{t2} are determined from the zigzag dependence of $h_c(Pr)$ (see figure 4) and both have a scaling of $\sim Ra^{-0.27\pm0.02}$.
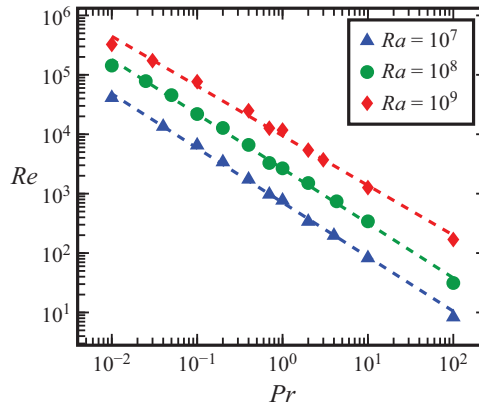

Figure 12. Log–log plot of the Reynolds number Re as a function of Pr for $Ra = 10^7$ (triangles), $Ra = 10^8$ (circles) and $Ra = 10^9$ (diamonds) obtained in the smooth cell. Here, the Reynolds number in our simulations is calculated as $Re = U_{rms}H/\nu$. The dashed lines are the best power-law fits to the corresponding data. The fitted scaling exponents are similar, but decrease with Rayleigh number from 0.9 ± 0.03 for $Ra = 10^7$ and 0.91 ± 0.03 for $Ra = 10^8$ to 0.84 ± 0.03 for $Ra = 10^9$.

In figure 11, we present the explored control parameters and a quantitative division of phase space based on the zigzag dependence of $h_c(Pr)$ (as shown in figure 4). Three regimes are separated by two transitional Prandtl numbers Pr_{t1} and Pr_{t2} (see the two dashed lines in figure 11), both of which follow a similar scaling $\sim Ra^{0.27\pm0.02}$. This implies that both transitions are governed by the same mechanism. As discussed above, the plume dynamics may be the possible mechanism that determines the transitions. On the basis of this view, we are now in a position to understand the scaling that separates the three regimes. In turbulent thermal convection, thermal plumes are subject to two kinds of dissipation: one is thermal dissipation and the other is viscous dissipation. When thermal dissipation is faster, plumes much more easily lose their thermal energy and coherence, and then they either hardly appear in the convective bulk or are entrained by the large-scale flows. In this situation, the convective bulk is dominated by the large-scale flows. On the other hand, when viscous dissipation is faster, the flows much more easily lose their kinetic energy, and plumes can sustain their thermal energy (as well defined thermal structures)

911 A52-14

for a long time and hence become more prominent in the system. Therefore, the transition can be quantified by the balance between the viscous dissipation time $\tau_u = U^2/\varepsilon_u$ and the thermal dissipation time $\tau_\theta = \Delta^2/\varepsilon_\theta$, where U is the typical velocity, and ε_u and ε_θ are the viscous and thermal dissipation rates, respectively. By making use of the two exact relations of the dissipation rates $\varepsilon_u = \nu^3 H^{-4} Nu Ra Pr^{-2}$ and $\varepsilon_\theta = \kappa H^{-2}\Delta^2 Nu$ (Ahlers *et al.* 2009), and the definition of the Reynolds number $Re = UH/\nu$, one can obtain $Re^2 \sim Ra Pr^{-1}$. According to previous results of $Re \sim Ra^{0.6}$ in 2-D turbulent RB convection (Sugiyama *et al.* 2009; Zhang, Zhou & Sun 2017), together with our present results of $Re \sim Pr^{-0.88\pm0.04}$ (as shown in figure 12), the balance between τ_u and τ_θ yields $Pr_t \sim Ra^{0.26\pm0.03}$, which agrees remarkably well with that of $Pr_{t1}, Pr_{t2} \sim Ra^{0.27\pm0.02}$ in figure 11, within uncertainty.

4. Conclusion

In summary, we have made a numerical exploration of 2-D turbulent RB convection over rough conducting plates. The critical roughness height h_c, denoting the onset of heat-transport enhancement owing to the wall roughness, is systematically investigated over a wide range of Prandtl number, with $10^7 \leqslant Ra \leqslant 10^9$ and $0.01 \leqslant Pr \leqslant 100$. Three regimes of $h_c(Pr)$ are identified in the phase diagram. For low Pr, the global Nu is mainly determined by molecular transport and decreases with descending Pr, resulting in the thickening of thermal BLs. This makes thermal BLs harder to be disrupted by rough elements and leads to a large h_c at small Pr. For medium Pr, the corner-flow rolls begin to be well developed due to the emergence of thermal plumes. The enhancement of the corner-flow strength and the increase of fluid viscosity both make h_c increase with Pr in this regime. For high Pr, the convective flow becomes dominated by thermal plumes. Since the rough elements can trigger massive eruptions of thermal plumes, it is much easier for the wall roughness to enhance the global Nu, leading to a small h_c at large Pr. Our detailed analysis further reveals that the plume dynamics plays a crucial role in the transitions among the three regimes.

Author ORCIDs.
Quan Zhou https://orcid.org/0000-0002-0411-7228.

REFERENCES

AHLERS, G., GROSSMANN, S. & LOHSE, D. 2009 Heat transfer and large scale dynamics in turbulent Rayleigh–Bénard convection. *Rev. Mod. Phys.* **81**, 503–537.

BAO, Y., CHEN, J., LIU, B.-F., SHE, Z.-S., ZHANG, J. & ZHOU, Q. 2015 Enhanced heat transport in partitioned thermal convection. *J. Fluid Mech.* **784**, R5.

BREUER, M., WESSLING, S., SCHMALZL, J. & HANSEN, U. 2004 Effect of inertia in Rayleigh–Bénard convection. *Phys. Rev.* E **69**, 026302.

CHANDRA, M. & VERMA, M.K. 2013 Flow reversals in turbulent convection via vortex reconnections. *Phys. Rev. Lett.* **110**, 114503.

CHILLÀ, F. & SCHUMACHER, J. 2012 New perspectives in turbulent Rayleigh–Bénard convection. *Eur. Phys. J.* E **35**, 58.

CILIBERTO, S. & LAROCHE, C. 1999 Random roughness of boundary increases the turbulent convection scaling exponent. *Phys. Rev. Lett.* **82**, 3998–4001.

DU, Y.-B. & TONG, P. 1998 Enhanced heat transport in turbulent convection over a rough surface. *Phys. Rev. Lett.* **81**, 987–990.

DU, Y.-B. & TONG, P. 2000 Turbulent thermal convection in a cell with ordered rough boundaries. *J. Fluid Mech.* **407**, 57–84.

DUBRULLE, B. 2002 Scaling in large Prandtl number turbulent thermal convection. *Eur. Phys. J.* B **28**, 361–367.

EMRAN, M.S. & SHISHKINA, O. 2020 Natural convection in cylindrical containers with isothermal ring-shaped obstacles. *J. Fluid Mech.* **882**, A3.

FOROOZANI, N., NIEMELA, J.J., ARMENIO, V. & SREENIVASAN, K.R. 2019 Turbulent convection and large scale circulation in a cube with rough horizontal surfaces. *Phys. Rev.* E **99**, 033116.

FRICK, P., KHALILOV, R., KOLESNICHENKO, I., MAMYKIN, A., PAKHOLKOV, V., PAVLINOV, A. & ROGOZHKIN, S. 2015 Turbulent convective heat transfer in a long cylinder with liquid sodium. *Europhys. Lett.* **14002**, 1–6.

GROSSMANN, S. & LOHSE, D. 2004 Fluctuations in turbulent Rayleigh–Bénard convection: the role of plumes. *Phys. Fluids* **16**, 4462–4472.

GROSSMANN, S. & LOHSE, D. 2008 Thermal convection in small Prandtl number liquids: strong but ineffective. *AIP Conf. Proc.* **1076**, 68.

GROSSMANN, S. & LOHSE, D. 2011 Multiple scaling in the ultimate regime of thermal convection. *Phys. Fluids* **23**, 045108.

HE, X.-Z., FUNFSCHILLING, D., NOBACH, H., BODENSCHATZ, E. & AHLERS, G. 2012 Transition to the ultimate state of turbulent Rayleigh–Bénard convection. *Phys. Rev. Lett.* **108**, 024502.

HORANYI, S., KREBS, L. & MÜLLER, U. 1999 Turbulent Rayleigh–Bénard convection in low-Prandtl number. *Intl J. Heat Mass Transfer* **42**, 3983–4003.

HOWARD, L.N. 1963 Heat transport by turbulent convection. *J. Fluid Mech.* **17**, 405–432.

HUANG, Y.-X. & ZHOU, Q. 2013 Counter-gradient heat transport in two-dimensional turbulent Rayleigh–Bénard convection. *J. Fluid Mech.* **737**, R3.

JIANG, H., ZHU, X., MATHAI, V., VERZICCO, R., LOHSE, D. & SUN, C. 2018 Controlling heat transport and flow structures in thermal turbulence using ratchet surfaces. *Phys. Rev. Lett.* **120**, 044501.

KACZOROWSKI, M. & XIA, K.-Q. 2013 Turbulent flow in the bulk of Rayleigh–Bénard convection: small-scale properties in a cubic cell. *J. Fluid Mech.* **722**, 596–617.

KRAICHNAN, R.H. 1962 Turbulent thermal convection at arbritrary Prandtl number. *Phys. Fluids* **5**, 1374–1389.

LEPOT, S., AUMAÎTRE, S. & GALLET, B. 2018 Radiative heating achieves the ultimate regime of thermal convection. *Proc. Natl Acad. Sci. USA* **115**, 8937–8941.

LIOT, O., EHLINGER, Q., RUSAOUEN, E., COUDARCHET, T., SALORT, J. & CHILLÀ, F. 2017 Velocity fluctuations and boundary layer structure in a rough Rayleigh–Bénard cell filled with water. *Phys. Rev. Fluids* **2**, 044605.

LOHSE, D. & XIA, K.-Q. 2010 Small-scale properties of turbulent Rayleigh–Bénard convection. *Annu. Rev. Fluid Mech.* **42**, 335–64.

MACDONALD, M., HUTCHINS, N., LOHSE, D. & CHUNG, D. 2019 Heat transfer in rough-wall turbulent thermal convection in the ultimate regime. *Phys. Rev. Fluids* **4**, 071501(R).

MALKUS, M.V.R. 1954 The heat transport and spectrum of thermal turbulence. *Proc. R. Soc. Lond.* A **225**, 196–212.

PANDEY, A. & VERMA, M.K. 2016 Scaling of large-scale quantities in Rayleigh–Bénard convection. *Phys. Fluids* **28**, 095105.

VAN DER POEL, E.P., STEVENS, R.J.A.M. & LOHSE, D. 2013 Comparison between two- and three-dimensional Rayleigh–Bénard convection. *J. Fluid Mech.* **736**, 177–194.

PRIESTLY, C.H.B. 1954 Convection from a large horizontal surface. *Austral. J. Phys.* **7**, 176–201.

DU PUITS, R., RESAGK, C. & THESS, A. 2010 Measurements of the instantaneous local heat flux in turbulent Rayleigh–Bénard convection. *New J. Phys.* **12**, 075023.

QIU, X.-L., XIA, K.-Q. & TONG, P. 2005 Experimental study of velocity boundary layer near a rough conducting surface in turbulent natural convection. *J. Turbul.* **6**, 30.

ROCHE, R.-E., CASTAING, B., CHABAUD, B. & HEBRAL, B. 2001 Observation of the 1/2 power law in Rayleigh–Bénard convection. *Phys. Rev.* E **63**, 045303(R).

ROCHE, P.-E., GAUTHIER, F., KAISER, R. & SALORT, J. 2010 On the triggering of the Ultimate Regime of convection. *New J. Phys.* **12**, 085014.

RUSAOUEN, E., LIOT, O., CASTAING, B., SALORT, J. & CHILLÀ, F. 2018 Thermal transfer in Rayleigh–Bénard cell with smooth or rough boundaries. *J. Fluid Mech.* **837**, 443–460.

SALORT, J., LIOT, O., RUSAOUEN, E., SEYCHELLES, F., TISSERAND, J.-C., CREYSSELS, M., CASTAING, B. & CHILLÀ, F. 2014 Thermal boundary layer near roughnesses in turbulent Rayleigh–Bénard convection: flow structure and multistability. *Phys. Fluids* **26**, 015112.

SCHEEL, J.D. & SCHUMACHER, J. 2016 Global and local statistics in turbulent convection at low Prandtl numbers. *J. Fluid Mech.* **802**, 147–173.

SHANG, X.-D., TONG, P. & XIA, K.-Q. 2008 Scaling of the local convective heat flux in turbulent Rayleigh–Bénard convection. *Phys. Rev. Lett.* **100**, 244503.

SHISHKINA, O., HORN, S., WAGNER, S. & CHING, E.S.C. 2015 Thermal boundary layer equation for turbulent Rayleigh–Bénard convection. *Phys. Rev. Lett.* **114**, 114302.

SHISHKINA, O. & WAGNER, C. 2011 Modelling the influence of wall roughness on heat transfer in thermal convection. *J. Fluid Mech.* **686**, 568–582.

SILANO, G., SREENIVASAN, K.R. & VERZICCO, R. 2010 Numerical simulations of Rayleigh–Bénard convection for Prandtl numbers between 10^{-1} and 10^4 and Rayleigh numbers between 10^5 and 10^9. *J. Fluid Mech.* **662**, 409–446.

SPIEGEL, E.A. 1971 Convection in stars. *Annu. Rev. Astron. Astrophys.* **9**, 323–352.

STEVENS, R.J.A.M., LOHSE, D. & VERZICCO, R. 2011 Prandtl and Rayleigh number dependence of heat transport in high Rayleigh number thermal convection. *J. Fluid Mech.* **688**, 31–43.

STRINGANO, G., PASCAZIO, G. & VERZICCO, R. 2006 Turbulent thermal convection over grooved plates. *J. Fluid Mech.* **557**, 307–336.

SUGIYAMA, K., CALZAVARINI, E., GROSSMANN, S. & LOHSE, D. 2009 Flow organization in two-dimensional non-Oberbeck-Boussinesq Rayleigh–Bénard convection in water. *J. Fluid Mech.* **637**, 105–135.

SUGIYAMA, K., NI, R., STEVENS, R.J.A.M., CHAN, T.-S., ZHOU, S.-Q., XI, H.-D., SUN, C., GROSSMANN, S., XIA, K.-Q. & LOHSE, D. 2010 Flow reversals in thermally driven turbulence. *Phys. Rev. Lett.* **105**, 034503.

SUN, C. & ZHOU, Q. 2014 Experimental techniques for turbulent Taylor–Couette flow and Rayleigh–Bénard convection. *Nonlinearity* **27**, R89–R121.

TISSERAND, J.-C., CREYSSELS, M., GASTEUIL, Y., PABIOU, H., GIBERT, M., CASTAING, B. & CHILLÀ, F. 2011 Comparison between rough and smooth plates within the same Rayleigh–Bénard cell. *Phys. Fluids* **23**, 015105.

TOPPALADODDI, S., SUCCI, S. & WETTLAUFER, J.S. 2015 Tailoring boundary geometry to optimize heat transport in turbulent convection. *Europhys. Lett.* **111**, 44005.

TOPPALADODDI, S., SUCCI, S. & WETTLAUFER, J.S. 2017 Roughness as a route to the ultimate regime of thermal convection. *Phys. Rev. Lett.* **118**, 074503.

VERZICCO, R. & CAMUSSI, R. 1999 Prandtl number effects in convective turbulence. *J. Fluid Mech.* **383**, 55–73.

WANG, Z., MATHAI, V. & SUN, C. 2019 Self-sustained biphasic catalytic particle turbulence. *Nat. Commun.* **10**, 3333.

WANG, B.-F., ZHOU, Q. & SUN, C. 2020 Vibration-induced boundary-layer destabilization achieves massive heat-transport enhancement. *Sci. Adv.* **6**, eaaz8239.

WEI, P., CHAN, T.-S., NI, R., ZHAO, X.-Z. & XIA, K.-Q. 2014 Heat transport properties of plates with smooth and rough surfaces in turbulent thermal convection. *J. Fluid Mech.* **740**, 28–46.

WHITEHEAD, J.P. & DOERING, C.R. 2011 Ultimate state of two-dimensional Rayleigh–Bénard convection between free-slip fixed-temperature boundaries. *Phys. Rev. Lett.* **106**, 244501.

XI, H.-D., LAM, S. & XIA, K.-Q. 2004 From laminar plumes to organized flows: the onset of large-scale circulation in turbulent thermal convection. *J. Fluid Mech.* **503**, 47–56.

XIA, K.-Q., LAM, S. & ZHOU, S.-Q. 2002 Heat-flux measurement in high-Prandtl-number turbulent Rayleigh–Bénard convection. *Phys. Rev. Lett.* **88**, 064501.

XIA, K.-Q., XIN, Y.-B. & TONG, P. 1995 Dual-beam incoherent cross-correlation spectroscopy. *J. Opt. Soc. Am.* A **12**, 1571.

XIE, Y.-C. & XIA, K.-Q. 2017 Turbulent thermal convection over rough plates with varying roughness geometries. *J. Fluid Mech.* **825**, 573–599.

XIN, Y.-B., XIA, K.-Q. & TONG, P. 1996 Measured velocity boundary layers in turbulent convection. *Phys. Rev. Lett.* **77**, 1266–1269.

Xu, A., Shi, L. & Xi, H.-D. 2019 Statistics of temperature and thermal energy dissipation rate in low-Prandtl number turbulent thermal convection. *Phys. Fluids* **31**, 125101.

Xu, B.-L., Wang, Q., Wan, Z.-H., Yan, R. & Sun, D.-J. 2018 Heat transport enhancement and scaling law transition in two-dimensional Rayleigh–Bénard convection with rectangular-type roughness. *Intl J. Heat Mass Transfer* **121**, 872–883.

Zhang, Y.-Z., Sun, C., Bao, Y. & Zhou, Q. 2018 How surface roughness reduces heat transport for small roughness heights in turbulent Rayleigh–Bénard convection. *J. Fluid Mech.* **836**, R2.

Zhang, Y.-Z., Xia, S.-N., Dong, Y.-H., Wang, B.-F. & Zhou, Q. 2019 An efficient parallel algorithm for dns of buoyancy-driven turbulent flows. *J. Hydrodyn.* **31** (6), 1159–1169.

Zhang, Y., Zhou, Q. & Sun, C. 2017 Statistics of kinetic and thermal energy dissipation rates in two-dimensional turbulent Rayleigh–Bénard convection. *J. Fluid Mech.* **814**, 165–184.

Zhou, Q. & Xia, K.-Q. 2013 Thermal boundary layer structure in turbulent Rayleigh–Bénard convection in a rectangular cell. *J. Fluid Mech.* **721**, 199–224.

Zhu, X., Jiang, L.-F., Zhou, Q. & Sun, C. 2019*a* Turbulent Rayleigh–Bénard convection in an annular cell. *J. Fluid Mech.* **869**, R5.

Zhu, X.-J., Stevens, R.J.A.M., Shishkina, O., Verzicco, R. & Lohse, D. 2019*b* $Nu \sim Ra^{1/2}$ scaling enabled by multiscale wall roughness in Rayleigh–Bénard turbulence. *J. Fluid Mech.* **869**, R4.

Zhu, X.-J., Stevens, R.J.A.M., Verzicco, R. & Lohse, D. 2017 Roughness-facilitated local 1/2 scaling does not imply the onset of the ultimate regime of thermal convection. *Phys. Rev. Lett.* **119**, 154501.

Zwirner, L. & Shishkina, O. 2018 Confined inclined thermal convection in low-Prandtl-number fluids. *J. Fluid Mech.* **850**, 984–1008.